

Experimental Investigation of Enhanced Grooves for Herringbone Grooved Journal Bearings

Philipp K. Bättig

Laboratory for Applied Mechanical Design (LAMD),

Department of Mechanical Engineering,
Ecole Polytechnique Fédérale de Lausanne,
CH-2002 Neuchâtel 2, Switzerland
e-mail: philipp.baettig@gmx.ch

Patrick H. Wagner

Laboratory for Applied Mechanical Design (LAMD),

Department of Mechanical Engineering,
Ecole Polytechnique Fédérale de Lausanne,
CH-2002 Neuchâtel 2, Switzerland
e-mail: mail@patrick-wagner.net

Jürg A. Schiffmann

Laboratory for Applied Mechanical Design (LAMD),

Department of Mechanical Engineering,
Ecole Polytechnique Fédérale de Lausanne,
CH-2002 Neuchâtel 2, Switzerland
e-mail: jurg.schiffmann@epfl.ch

This paper presents the results of a theoretical and experimental investigation of the potential of enhanced groove geometries to increase the bearing clearance of a Herringbone Grooved Journal Bearing (HGJB) supported rotor. The theoretical study investigates various groove geometries of different complexities and their effect on the stability threshold of a particular rotor geometry. The theoretical results obtained from a rigid-body rotordynamic model suggest an increase of more than 300% in instability onset speed when enhanced groove geometries are used compared to a classical, helically grooved rotor featuring the same radial bearing clearance. As part of the experimental investigation, one rotor shaft with classical grooves, representing the baseline rotor, and four rotors of identical diameter and clearance, but featuring enhanced grooves of varying degrees of complexity, were manufactured and experimentally tested. Good agreement between the experimentally determined speed of instability onset and the prediction was found for the investigated enhanced groove patterns. Experimental results of the classical rotor suggest the onset of instability to occur at a rotational speed of 56 krpm, whereas a speed of 180 krpm was achieved when enhanced groove geometries were applied to the rotor, which agrees very well with the theoretically predicted results and confirms the potential of enhanced groove geometries to stabilize HGJBs. Furthermore, the rotor featuring only a varying groove angle along the rotor axis was found to perform similarly to fully enhanced grooves of varying groove width, depth, and angle, hence representing a good trade-off between performance increase and design cost. [DOI: 10.1115/1.4053978]

Keywords: bearing design and technology, gas (air) bearings, hydrodynamic lubrication

1 Introduction

Various researchers have investigated ways to increase the stability threshold of Herringbone Grooved Journal Bearings (HGJBs), which would allow a relaxation in the stringent manufacturing tolerances and hence the cost of manufacturing. All investigated solutions that successfully increase the stability threshold of the rotor-bearing system work on the principle of inducing damping. Increasing the stability threshold of HGJBs by means of introducing external damping to the bearing bushing has been presented by flexibly supporting the bearing bushings on elastomeric O-Rings [1–7] or by using flexible structures that provide Coulomb damping [8–10]. Both methods have shown promising results to increase the stability threshold of HGJBs.

Another way of inducing damping to the rotor-bearing system is the alteration of the gas film itself by means of optimized groove geometries to improve the rotordynamic bearing performance. Conventional HGJB groove geometries feature constant groove angle β , width ratio α , and depth ratio H along the rotor axis. The application of optimized groove geometries was followed by a number of researchers, namely, Ikeda et al. [11], who investigated the effect of non-uniform grooves by defining grooves that change linearly in the axial rotor direction. The authors compare a rotor with classical grooves to a rotor featuring enhanced grooves of varying depth, width, and angle along the rotor axis. The experimental investigation suggested that by using enhanced grooves, the

maximum rotational speed before instability occurs could be increased by 20% compared to a classical groove pattern.

Schiffmann [12] performed multi-objective optimizations of enhanced groove geometries for a particular rotor geometry on rigidly supported bearing bushings, suggesting a possible increase in bearing clearance by up to 80%, while maintaining the same rotordynamic stability.

The potential of enhanced groove geometries was also investigated for spiral-grooved thrust bearings, namely, by Hashimoto and Ochiai [13], who found that a spline-shaped groove geometry is able to significantly increase the stiffness and stability of a hydrodynamic gas film thrust bearing compared to conventionally used logarithmic spiral-grooved thrust bearings. A very recent work by Yu et al. [14] found that a herringbone-grooved thrust bearing optimized in various sections was able to offer 30.77% higher load capacity than a regular thrust bearing groove patterns, which were corroborated by experimental results.

1.1 Motivation and Nature of the Issue. Gas bearing supported rotors for high-speed turbomachinery are usually manufactured from materials like high-strength steel, ceramics, or tungsten carbide due to their favorable ratio of elastic modulus to density, as well as high mechanical strength. The raw materials, manufacturing and assembly requires considerable financial investment and there is a clear interest in a reduction of waste parts failing quality control. The matching of rotors and bearing bushings is a viable option in the production of large batches and can help to reduce waste by matching rotor–bushing pairs. However, remaining rotors or bushings that do not respect the manufacturing tolerances and cannot be saved by part-matching due to too large clearances could potentially be saved with the application of enhanced

Contributed by the Tribology Division of ASME for publication in the JOURNAL OF TRIBOLOGY. Manuscript received March 19, 2021; final manuscript received December 8, 2021; published online March 18, 2022. Assoc. Editor: Alan Palazzolo.

groove geometries, resulting in a further reduction in cost. In addition to the previously presented benefits that come with an increase in bearing clearance, the application of enhanced groove geometries offers the advantage of increased bearing performance for almost no additional cost.

The theoretical investigation performed by Schiffmann [12] suggests very promising results for the application of enhanced groove geometries in HGJB supported rotors. However, there is no experimental validation of the effect of enhanced groove geometries for HGJBs except the one by Ikeda et al. [11], who performed a theoretical and experimental investigation of one rotor featuring varying groove depth, width, and angle.

Multi-objective optimizations require high computational resources, which roughly increase linearly with the number of variables to be optimized [15]. The optimization of a fully enhanced groove design, featuring variable groove angle β , groove width ratio α , and groove depth ratio H , whose values are defined at four interpolation points along the z -axis, requires the optimization of 12 design variables. In case the same performance enhancement is achievable with an enhanced groove design of reduced complexity, the computational resources could be reduced significantly. Furthermore, the manufacturing of fully enhanced grooves with varying α , β , and H along the rotor axis can lead to an increase in cost of laser-grooving, if the average groove depth is deeper compared to classical grooves.

In order to save computational resources and design/manufacturing cost, the identification of the groove design variables that are offering the highest performance with increased potential is of high interest.

1.2 Goals and Objectives. The objectives of this paper are (1) to perform a theoretical investigation of the potential of enhanced grooves to increase the bearing clearance while maintaining rotordynamic stability for a rigidly supported rotor, (2) to design, manufacture, and experimentally analyze five rotors featuring varying degrees of enhanced groove complexity and compare the results to a classically grooved rotor, (3) to experimentally validate the simulation codes for gas bearings featuring enhanced groove geometries, and (4) to identify groove parameters suggested to offer the highest potential to increase stability and/or bearing clearance.

1.3 Scope of the Paper. In a first step, a theoretical model for the rotordynamic system and the procedure to solve the narrow-groove-theory (NGT) for non-helical grooves is presented, which allows to determine the speed of instability onset (SIO) for a rigidly supported rotor on HGJBs with enhanced grooves. In a second step, a theoretical investigation featuring multi-objective optimizations is performed to investigate the potential of enhanced groove geometries to increase the bearing clearance. In addition, an analysis of various groove parameters is conducted to study which parameter offers the highest potential to increase the bearing clearance. In a third step, the experimental setup and the data treatment procedure are presented that allow to experimentally investigate the speed of instability onset for the different groove geometries. In a fourth step, five rotors featuring groove geometries of different complexities with the same radial bearing clearance are experimentally tested up to the onset of instability to compare the obtained results to the numerical models, followed by a discussion of the experimental and numerical results including the identification of groove parameters offering the highest potential to increase the bearing clearance.

2 Methodology

2.1 Numerical Modeling. The rigid-body rotordynamic system that is used to predict the whirl speed and stability maps is presented in Fig. 1 and can be described by Eq. (1), where M

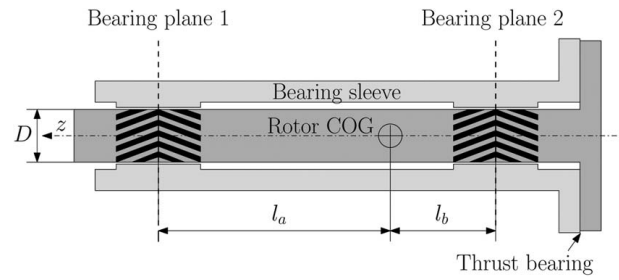


Fig. 1 Rotordynamic model used for multi-objective optimizations

is the inertia matrix of the system, K is the matrix containing the bearing stiffness values, and B is the damping matrix containing the bearing damping coefficients as well as the gyroscopic effects.

$$K\vec{q} + B\dot{\vec{q}} + M\ddot{\vec{q}} = \vec{F} \quad (1)$$

with

$$\vec{q} = [x, y, \alpha, \beta]^T \quad (2)$$

where x and y correspond to the translational and α and β to the rotational motion of the rigid-body rotor at the center of gravity (COG). The rotordynamic properties of the rigid-body rotor-bearing system are described in terms of rotor mass m_{Rot} , polar and transverse rotor inertia J_p and J_T , and by the distance of bearing mid-planes relative to the rotor center of gravity l_a and l_b . The details of the system inertia, stiffness, and damping matrices in Eq. (1) are given in the annex. Equation (1) yields an eigenvalue problem with eigenvalues defined in Eq. (3).

$$s_j = \lambda_j + i\Omega_j\omega_{\text{Rot}} \quad (3)$$

The imaginary part $\omega_j = \Omega_j\omega_{\text{Rot}}$ represents the damped natural frequency of the whirl motion and λ_j is the corresponding damping coefficient. The rotordynamic stability is evaluated using the logarithmic decrement Γ , which is defined as

$$\Gamma_j = -\lambda_j \frac{2\pi}{\Omega_j\omega_{\text{Rot}}} \quad (4)$$

Stable rotor operation requires positive logarithmic decrements at all rotor speeds between zero and the nominal rotor speed N_{Rot} . The four degrees-of-freedom of the rigid-body system yield forward and backward cylindrical and conical rotor vibration modes. Table 1 presents the rotor and bearing properties of the investigated rotor to perform the theoretical and experimental enhanced groove geometry exploration.

Table 1 Rotor design properties and operating conditions for theoretical and experimental enhanced groove geometry exploration

Bearing diameter, D	8 mm
Bearing length-to-diameter ratio, L/D	1
Rotor mass, m_{Rot}	0.0271 kg
Polar rotor inertia, J_p	$6.073 \times 10^{-7} \text{ kg m}^2$
Transverse rotor inertia, J_T	$7.782 \times 10^{-6} \text{ kg m}^2$
Bearing distance, l	24.78 mm
Distance from front bearing to rotor COG, l_a	8.65 mm
Distance from back bearing to rotor COG, l_b	16.13 mm
Nominal rotor speed, N_{Rot}	180 krpm
Ambient lubricant pressure, p_{amb}	101.3 kPa
Ambient lubricant temperature, T_{amb}	298 K
Lubricant viscosity, μ	18 $\mu\text{Pa s}$

The prediction of the eigenfrequencies and the corresponding damping of the rigid-body rotor system require the input of the bearing impedance (stiffness and damping). For the analysis in this paper, an adapted narrow-groove-theory (NGT) for non-helical grooves presented by Schiffmann [12] is used and given as follows:

$$\begin{aligned} \partial_\theta [\bar{P} \partial_\theta (f_1 \bar{P}) + \bar{P} \partial_z (f_2 \bar{P})] + \partial_z [\bar{P} \partial_\theta (f_2 \bar{P}) + \bar{P} \partial_z (f_3 \bar{P})] \\ + [\partial_\theta (c_s \sin \beta \bar{P} f_4) - \partial_z (c_s \cos \beta \bar{P} f_4)] \\ - \Lambda \partial_\theta (\bar{P} f_5) - \sigma \partial_z (\bar{P} f_5) = 0 \end{aligned} \quad (5)$$

where the geometrical variables f_i and c_s as well as the operational ones Λ and σ are summarized in the annex. The fluid film is perturbed following the approach by Lund [16] in view of computing the linearized bearing impedance:

$$\bar{h} = 1 + \varepsilon_x \cos \theta e^{i\bar{t}} + \varepsilon_y \sin \theta e^{i\bar{t}} \quad (6)$$

leading to a perturbation of the fluid film pressure as follows:

$$\bar{P} = \bar{P}_0 + \varepsilon_x \bar{P}_x e^{i\bar{t}} + \varepsilon_y \bar{P}_y e^{i\bar{t}} \quad (7)$$

Using Eqs. (6) and (7) in Eq. (5) and collecting the zeroth- and first-order terms yields linearized differential equations for the unperturbed pressure \bar{P}_0 and for the two perturbed pressure contributions in x and y (\bar{P}_x and \bar{P}_y). The three linear differential equations are numerically integrated using a finite difference approach. Finally, the bearing impedance $Z = K + i\gamma \Omega_{\text{rot}} C$ is obtained by integrating the perturbed pressures within the fluid film and projecting the resulting force on the x -axis and y -axis, respectively:

$$\begin{aligned} Z_{xx} &= -R^2 p_{\text{amb}} \int_{-L/D}^{L/D} \int_0^{2\pi} \bar{P}_x \cos \theta d\theta d\bar{z} \\ Z_{yx} &= -R^2 p_{\text{amb}} \int_{-L/D}^{L/D} \int_0^{2\pi} \bar{P}_x \sin \theta d\theta d\bar{z} \\ Z_{yy} &= -R^2 p_{\text{amb}} \int_{-L/D}^{L/D} \int_0^{2\pi} \bar{P}_y \sin \theta d\theta d\bar{z} \\ Z_{xy} &= -R^2 p_{\text{amb}} \int_{-L/D}^{L/D} \int_0^{2\pi} \bar{P}_y \cos \theta d\theta d\bar{z} \end{aligned} \quad (8)$$

Further insights into the detailed derivation of the NGT are summarized in a review by Gu et al. [17], while a theoretical assessment of the validity and limitations of the NGT compared to a finite groove approach are given by Iseli et al. [18]. Furthermore, Guenat and Schiffmann [19] compared the NGT to experimentally measured bearing impedance suggesting a good agreement.

Figure 2 presents the cut-view (top) and an unwrapped view (bottom) of a herringbone-grooved journal bearing and the relevant design variables. In the case of enhanced grooves, the variables for groove width α , groove angle β , and groove depth ratio H evolve along the axial position z described here by a third-order polynomial expression using the interpolation points at Pos1 to Pos4, which are equally distributed within the grooved region. Pos1 refers to the position where the grooves start, in the bearing center $z=0$ for $\gamma=1$, while Pos4 is the position at the outer groove edge. The dimensionless variables for the groove depth ratio H , groove width ratio α , and bearing length ratio γ are defined in Eq. (9).

$$H = \frac{h_g}{C}, \quad \alpha = \frac{w_g}{w_g + w_r}, \quad \gamma = \frac{L - L_{\text{Land}}}{L} \quad (9)$$

In this work, the identification of the ideal groove patterns is formulated as a multi-objective optimization problem in view of maximizing both the logarithmic decrement and the nominal bearing clearance. The optimization is performed for five groove patterns of varying degrees of groove complexity, summarized as follows:

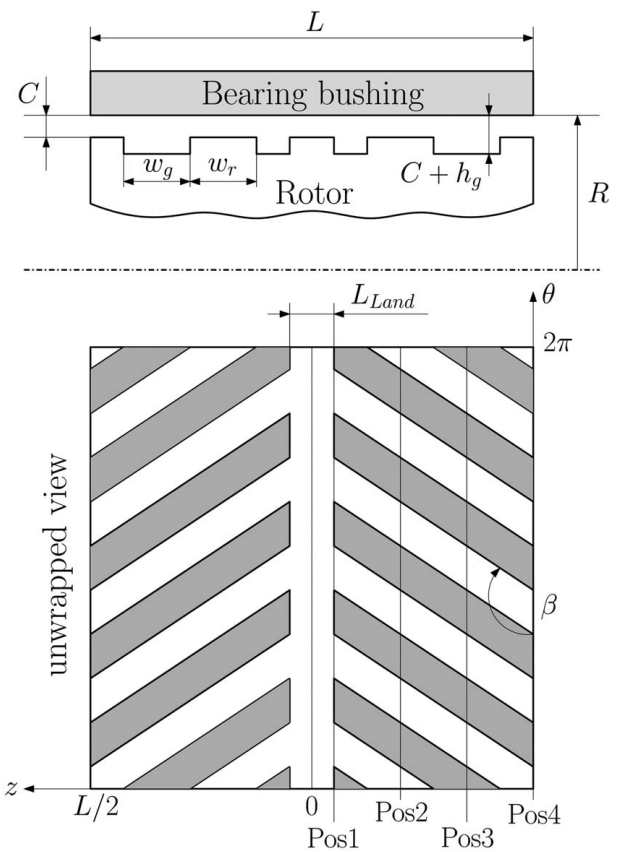


Fig. 2 Nomenclature of HGJB including the four interpolation points along the rotor axis to define the enhanced groove geometry

classic: straight grooves of constant groove width ratio α , constant groove angle β , and constant groove depth ratio H .

alpha_var: enhanced grooves with variable groove width ratio α , but constant groove angle β and constant groove depth ratio H .

beta_var: enhanced grooves with variable groove angle β , but constant groove width ratio α and constant groove depth ratio H .

alpha_beta_var: enhanced grooves with variable groove width ratio α and variable groove angle β , but constant groove depth ratio H .

alpha_beta_hg_var: enhanced grooves with variable groove width ratio α , variable groove angle β , and variable groove depth ratio H .

Note that groove parameters that are left constant along the rotor axis are also optimized individually for each rotor configuration. Table 2 presents the boundary conditions of the multi-objective optimizations performed for the rotor with the design properties and operating conditions summarized in Table 1. The optimization for identifying the ideal trade-off between the two competing

Table 2 Range of design variables for the performed multi-objective optimizations

Groove width ratio $\alpha \in$	[0.35, 0.65]
Groove angle $\beta \in$	[110, 170] deg
Groove depth ratio $H \in$	[1.0, 6.0]
Bearing length ratio $\gamma \in$	[0.5, 1.0]
Radial bearing clearance $C \in$	[3, 20] μm

Note: The numbers in brackets represent the minimum and maximum of the investigated range.

objectives (maximum stability versus. maximum clearance) is performed through an evolutionary algorithm developed by Molyneux et al. [20]. The process was started with a randomly distributed initial population of 500 individuals and stopped after convergence of both the Pareto curve and the evolution of the design variables, usually after 50,000 evaluations.

2.2 Experimental Setup. The experimental measurement campaign aims to identify the performance of various enhanced groove patterns by comparing the results to a baseline rotor featuring classical grooves of constant groove angle β , width ratio α , and depth ratio H . As a consequence, five rotors are manufactured with the groove patterns *classic*, *alpha_var*, *beta_var*, *alpha_beta_var*, and *alpha_beta_hg_var* and their performance experimentally evaluated in terms of their onset speed of instability. The number of grooves of all experimentally tested rotors is 16. The rotor properties presented in Table 1 correspond to the prototype rotor designed by Wagner et al. [21], which served as a proof-of-concept for a steam-driven micro-recirculation fan for solid oxide fuel cell systems.

The prototype is instrumented with four capacitive displacement probes, capturing rotor displacements in x - and y -direction both on the front (fan-side) and the back (turbine-side) bearing plane of the rotor shaft. An optical displacement probe is mounted on the stator part of the prototype facing the thrust disk of the rotor and captures a trigger mark, which provides information about the phase angles and rotational speed. Figure 3(a) presents the fan-side of the

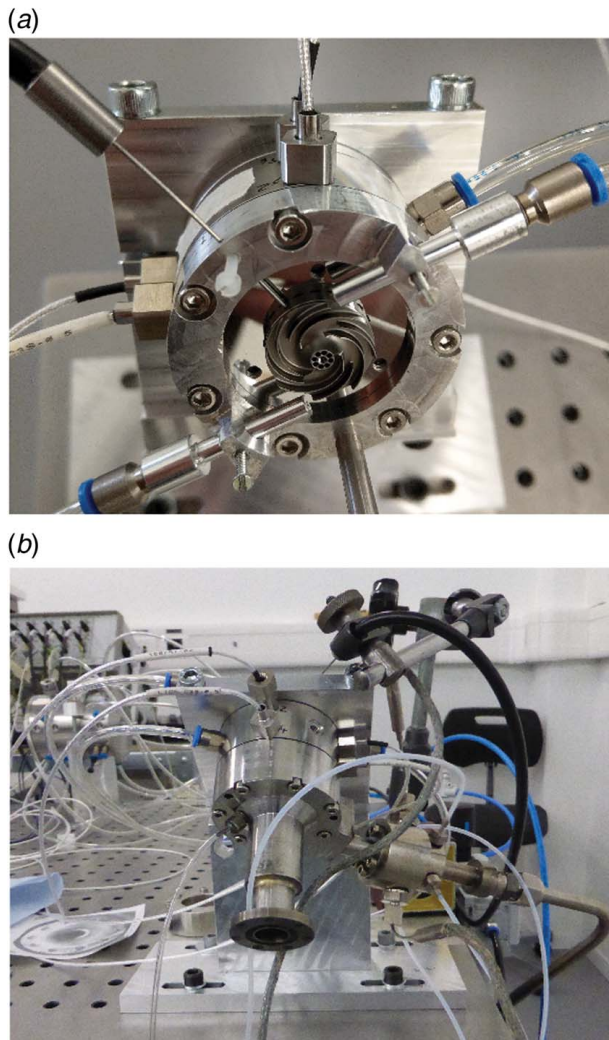


Fig. 3 Experimental setup for the enhanced groove exploration: (a) fan-side of rotor shaft and (b) turbine-side of rotor shaft

Table 3 List of instrumentation for the enhanced groove geometry exploration

Device	Model
Capacitive displacement probes	Lion precision C3S
Optical displacement probe	Philtec D20
Signal amplifier	Lion precision CPL290
Data acquisition system	NI PXIe-1078/6356

prototype used to experimentally investigate the effect of enhanced groove geometries lubricated with ambient air. Shown are the two nozzles that allow to drive the rotor by means of compressed air aimed at the fan, the optical Philtec probe, as well as the four capacitance probes. The turbine-side of the prototype is shown in Fig. 3(b) with the turbine volute mounted. Supplying compressed air to the turbine inlet allows for a second driving-mode to power the rotor shaft. As was found during the experimental campaign, the fan-driven operational mode allows smooth starting of the rotor but induces unwanted noise in the frequency spectrum of the rotor motion. The turbine-driven operational mode does not induce any unwanted vibrations; however, controlling the rotational speed is difficult at low speeds. A coupled operational scheme was therefore adapted that allows to smoothly start the rotor shaft by means of the fan and is then followed by a transition into the turbine-driven operational mode for high-speed measurements, free of any unwanted noise.

The signature of an unstable gas bearing supported rotor due to self-excited whirl is the presence of sub-synchronous vibrations [22,23]. Hence, it is common practice to measure the rotor orbits on two planes and to analyze their frequency spectrum. Furthermore, measurement of the rotor motion allows to balance the rotor shaft in situ using the influence coefficient method [24]. Table 3 summarizes the list of instruments used to perform the experimental investigation.

3 Results and Discussion

3.1 Results of Multi-Objective Optimizations. Figure 4 presents the Pareto front of the logarithmic decrement Γ against the radial clearance C for the rotor *classic* and the four rotors featuring enhanced groove geometries of increasing degree of complexity. The presented logarithmic decrement Γ corresponds to the lowest predicted value in the whole speed range up to the nominal rotor

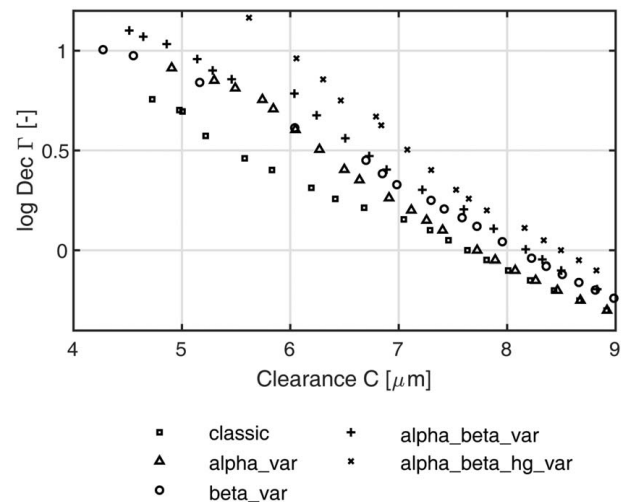


Fig. 4 Evolution of logarithmic decrement Γ for rotor *classic* and the four rotors featuring enhanced groove geometries of increasing degree of complexity

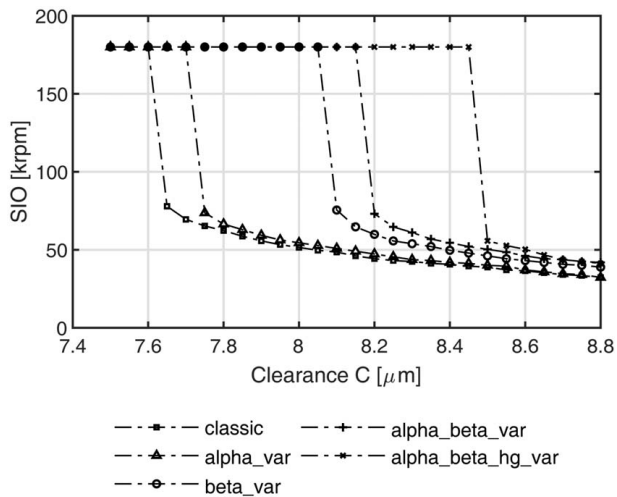


Fig. 5 Predicted speed of instability onset for the classically grooved rotor and the four rotors featuring enhanced groove geometries

speed of 180 krpm. The results presented in Fig. 4 suggest a possible increase in bearing clearance from $7.6 \mu\text{m}$ to $8.5 \mu\text{m}$ (12%) for neutral stability, using fully enhanced grooves. At lower clearances, fully enhanced grooves applied to this particular rotor geometry allow an increase in bearing clearance by up to 37%, while maintaining the same rotordynamic stability. This result is lower than the predicted increase of 80% by Schiffmann [12], which suggests that the potential gain of enhanced grooves is strongly dependent on the rotor mass, the transverse moment of inertia, and the relative location of the center of mass.

As is evident from the results presented in Fig. 4, the groove geometry *alpha_var* offers increased performance compared to the classically grooved rotor for low clearance levels; however, its ability to improve stability vanishes almost completely at clearances above $7.5 \mu\text{m}$. While not offering any increased performance at low clearances compared to the geometry *alpha_var*, the groove geometry *beta_var* presents an almost identical performance as *alpha_beta_var* for clearances above $6.5 \mu\text{m}$.

Furthermore, a maximum clearance C of $7.6 \mu\text{m}$ is required to ensure stable operation ($\Gamma > 0$) of the rotor *classic* up to the nominal rotor speed of 180 krpm. The maximum clearances for the enhanced groove geometries are $7.7 \mu\text{m}$, $8.1 \mu\text{m}$, $8.2 \mu\text{m}$, and $8.5 \mu\text{m}$ for the rotors *alpha_var*, *beta_var*, *alpha_beta_var*, and *alpha_beta_hg_var*, respectively.

In order to experimentally validate the theoretically obtained results, five rotor shafts with these nominal clearances would need to be manufactured. It is evident that even by using the most modern technologies available, manufacturing of differences in rotor diameter as small as $0.1 \mu\text{m}$ is very challenging and expensive. It was therefore decided to design all five rotors with the same diameter, resulting in the same radial bearing clearance for all rotors, and experimentally compare the different groove designs by increasing the rotational speed of each rotor until instability occurs. The obtained maximum rotational speed of each tested rotor then allows to compare the performance of the different groove patterns.

3.2 Identification of Common Bearing Clearance for Experimental Campaign.

Figure 5 presents the speed of instability onset (SIO), defined as the rotational speed where the logarithmic decrement becomes zero, as a function of the bearing clearance C for the rotor *classic* and the four rotors featuring enhanced grooves. The maximum speed in the experimental setup is limited to a nominal speed of $N_{\text{Rot}} = 180 \text{ krpm}$, which is why all predicted speeds of instability onset (SIO) were limited to 180 krpm in case the instability onset was predicted to be higher than 180 krpm. As suggested by the results presented in Fig. 5, the speed of instability onset (SIO) increases with decreasing clearance C for all rotors. Similar to the results for the logarithmic decrement Γ presented in Fig. 4, the SIO increases with increasing complexity of the applied groove pattern. Using the theoretically predicted results presented here, the objective is to define the ideal clearance for all rotors that offers the highest chance of experimentally capturing the different speeds of instability onset of the rotors to compare their performance.

In order to facilitate the selection of a common radial clearance C for all five rotors, the results from Fig. 5 are plotted in Fig. 6 presenting the speed of instability onset (SIO) as a function of radial bearing clearance C for the five bearing configurations.

The ideal clearance to be defined for all five rotors yields instability within the nominal speed range up to 180 krpm and ideally results in large enough differences in SIO to be captured in the experiment. Due to the fact that the nominal rotor speed of 180 krpm cannot be exceeded during the experimental measurement campaign, the ideal clearance is therefore suggested to be $C = 8.2 \mu\text{m}$. At this clearance, all rotors become unstable within the nominal speed range, except for rotor *alpha_beta_hg_var*, which is predicted to run in a stable manner up to the nominal speed of 180 krpm.

For an identical radial clearance of $C = 8.2 \mu\text{m}$, the predicted speed of instability onset for all five rotors is presented in Table 4. The optimized groove geometries for the five investigated

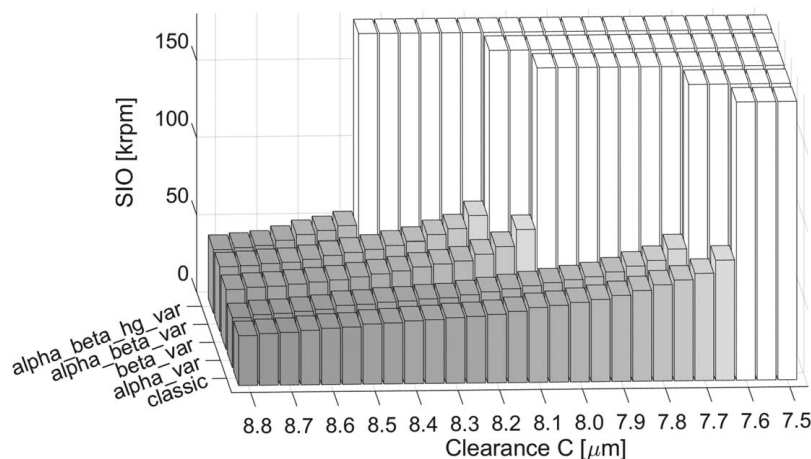


Fig. 6 Predicted speed of instability onset for rotor classic and the four rotors featuring enhanced groove geometries

Table 4 Predicted speed of instability onset (SIO) for all five investigated rotors with a radial clearance $C = 8.2 \mu\text{m}$

Rotor name	SIO (krpm)
<i>classic</i>	44
<i>alpha_var</i>	47
<i>beta_var</i>	60
<i>alpha_beta_var</i>	73
<i>alpha_beta_hg_var</i>	>180

rotors resulting from the multi-objective optimizations for a common radial bearing clearance of $C = 8.2 \mu\text{m}$ are summarized in Table 5. The optimization results suggest the optimum groove pattern to be fully grooved and features steep and shallow grooves in the bearing edge region, which become flatter and deeper towards the center region of the bearing.

Figure 7 shows the unperturbed fluid film pressures for the different bearing configurations as a function of the axial position with the fluid film computed for a rotor speed of 180 krpm. The counter-acting viscous pumping effect by the V-shaped grooves is highlighted by the raising pressure toward the bearing center. The classical groove geometry yields a perfectly linear evolution of the pressure, while the enhanced groove geometries lead to pressure profiles that deviate from a purely linear evolution. This deviation results in varying first-order derivatives and in non-zero second-order derivatives of the unperturbed pressure with regard to the axial coordinate, which influence the expressions for the perturbed pressures and therefore the bearing impedances. This is highlighted in Fig. 8, which represents the synchronous bearing impedance values for the different bearing configurations as a function of the bearing compressibility number. The curves suggest that the different groove patterns primarily affect the cross-coupled stiffness K_{xy} and the direct damping C_{xx} , which directly influence the stability of the bearings.

3.3 Manufacturing of Bearing Bushing and Rotors. One bearing bushing, suitably designed to test all five rotors of different groove patterns, has been manufactured from a heat treated stainless steel of grade 1.4125. Measurements of the bearing bushing were performed, which resulted in an internal diameter (ID) of 8.0106 mm, a roundness error of $0.2 \mu\text{m}$, and a parallelism error of $0.5 \mu\text{m}$. Five rotors were manufactured in an identical grade of steel to the diameter required for a clearance C of $8.2 \mu\text{m}$. With respect to the measured bearing bushing ID, the outer diameter (OD) of all five rotors is targeted to be $D_{\text{rot}} = 7.9942 \text{ mm}$. Measurements of the rotor diameters after manufacturing, as well as the resulting clearances for all rotors, are summarized in Table 6. The measurement uncertainty for the rotor diameter is $\pm 0.4 \mu\text{m}$. With a maximum difference of $0.05 \dots 0.2 \mu\text{m}$ ($0.6 \dots 2.4\%$) with respect to the nominal radial bearing

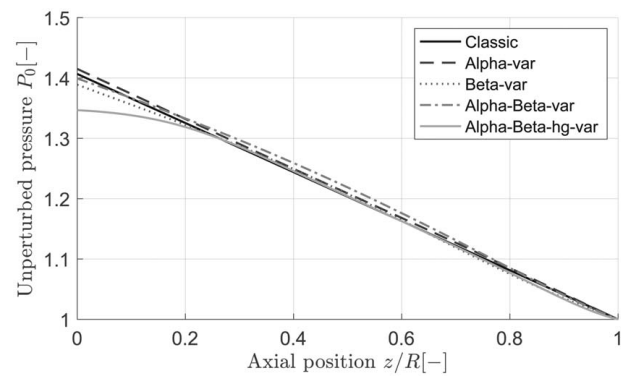


Fig. 7 Comparison of the unperturbed fluid film pressure as a function of the axial bearing position (0 = bearing center, 1 = bearing edge) computed at a rotor speed of 180 krpm

clearance of $C = 8.2 \mu\text{m}$, all rotors can be considered identical except for their groove pattern. Figure 9 presents the computer aided design (CAD) geometry of the optimized groove patterns for rotors *classic*, *alpha_var*, *beta_var*, *alpha_beta_var*, and *alpha_beta_hg_var* (from left to right), as well as the realized groove patterns for the experimental investigation after manufacturing by means of laser etching. The manufactured bearing bushing and the rotor components for the experimental investigation of enhanced groove geometries are presented in Fig. 10. The rotor components listed from left to right are nut, turbine, shim, tie bolt, rotor, and fan. The shim is required to adjust the axial rotor clearance.

3.4 Experimental Identification of the Speed of Instability Onset. Figure 11 presents the captured synchronous and sub-synchronous motion amplitudes on the front and the back bearing plane for rotor *classic* that serves as a baseline for the performance evaluation of the enhanced groove geometries. As suggested by the results presented in Fig. 11, the rotor *classic* shows a synchronous vibration amplitude on the front and the back bearing plane of about $0.5 \mu\text{m}$ at a rotor speed of 40 krpm after balancing. The evolution of the sub-synchronous motion amplitude shows very low values at low speed that slightly increase with increasing speed and then suddenly peak at 56 krpm. The captured sudden increase in sub-synchronous motion amplitude at the front and back of the rotor suggests the onset of instability of the rotor *classic* to be located at a rotational speed of 56 krpm.

Figure 12 shows the evolution of the synchronous and sub-synchronous rotor motion amplitudes captured for rotor *alpha_var*. The groove pattern of this rotor features a constant groove angle β , constant groove depth ratio H , but a variable groove width ratio α

Table 5 Optimized groove geometries of the investigated rotors for a radial clearance $C = 8.2 \mu\text{m}$

	<i>classic</i>	<i>alpha_var</i>	<i>beta_var</i>	<i>alpha_beta_var</i>	<i>alpha_beta_hg_var</i>
α_{Pos1}	0.65	0.65	0.65	0.65	0.65
α_{Pos2}	0.65	0.65	0.65	0.65	0.65
α_{Pos3}	0.65	0.65	0.65	0.65	0.65
α_{Pos4}	0.65	0.35	0.65	0.37	0.37
β_{Pos1}	146.2	147.2	137.7	136.0	116.8
β_{Pos2}	146.2	147.2	142.9	143.2	146.9
β_{Pos3}	146.2	147.2	158.7	156.5	151.3
β_{Pos4}	146.2	147.2	170.0	169.7	168.5
H_{Pos1}	1.62	1.73	1.92	1.93	6.0
H_{Pos2}	1.62	1.73	1.92	1.93	2.0
H_{Pos3}	1.62	1.73	1.92	1.93	1.5
H_{Pos4}	1.62	1.73	1.92	1.93	1.05
γ	1	1	1	1	1

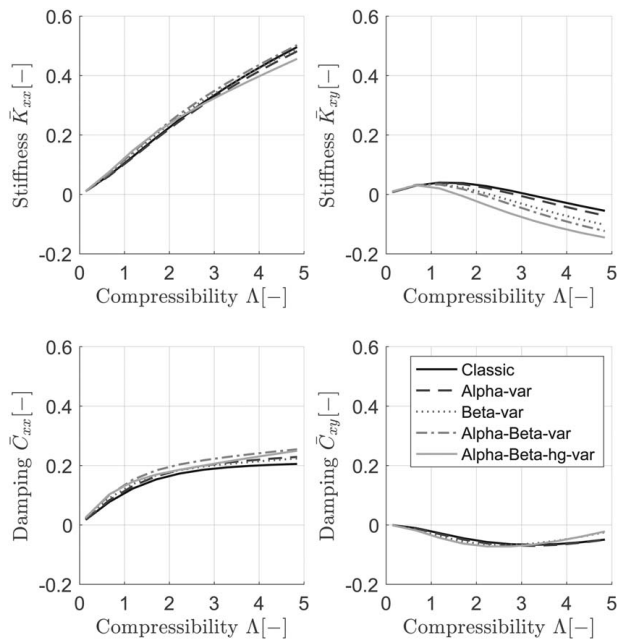


Fig. 8 Synchronous bearing impedance values for the different bearing configurations computed for a concentric bearing position as a function of the compressibility number

Table 6 Measurement results of rotor diameter

Rotor name	D_{rot} (mm)	Clearance C (μm)
<i>classic</i>	7.9938	8.4
<i>beta_var</i>	7.9938	8.4
<i>alpha_var</i>	7.9942	8.2
<i>alpha_beta_var</i>	7.9943	8.15
<i>alpha_beta_hg_var</i>	7.9943	8.15

along the rotor axis. As suggested by the recorded rotor amplitudes presented in Fig. 12, the rotor *alpha_var* exhibits elevated levels of sub-synchronous vibration on both the front and the back bearing location already at low speeds, suggesting a low level of stability for this groove pattern. In general, operation of the rotor *alpha_var* proved to be challenging (difficult speed regulation), most probably caused by the continuous onset and cessation of rotor instabilities. Nevertheless, a maximum rotational speed of 80 krpm was achieved with rotor *alpha_var* before the sub-synchronous vibration amplitudes intermittently exceeded the synchronous motion amplitudes. The experiment was stopped at this point to avoid failure of the rotor or bearing bushing.

The recorded synchronous and sub-synchronous rotor amplitudes for rotor *beta_var*, featuring a variable groove angle but constant



Fig. 10 Manufactured bearing bushing (top) and rotor (bottom) for enhanced groove geometry exploration. From left to right: nut, turbine, axial shim, tie bolt, and rotor with fan.

groove width and depth, are shown in Fig. 13. The evolution of sub-synchronous rotor amplitudes presented in Fig. 13 shows an increase with increasing rotational speed for the front and the back bearing. At a rotational speed of 120 krpm, the sub-synchronous vibration amplitude of the back bearing starts to increase progressively and peaks at $0.2 \mu\text{m}$ for a speed of 180 krpm. The sub-synchronous amplitude of the front bearing on the other hand levels out at a constant sub-synchronous amplitude of around $0.06 \mu\text{m}$. A maximum speed of 180 krpm was achieved with rotor *beta_var*; however, the increasing slope in the evolution of the sub-synchronous vibration amplitude on the back bearing after 160 krpm suggests the onset of instability to be situated at a rotor speed not far above 180 krpm.

The recorded results for rotor motion amplitude of rotor *alpha_beta_var* are presented in Fig. 14. As suggested by the results presented in Fig. 14, a maximum rotational speed of 180 krpm was achieved with rotor *alpha_beta_var*. The sub-synchronous motion amplitudes of rotor *alpha_beta_var* are generally at a lower level compared to rotor *beta_var*, indicating a higher stability threshold of rotor *alpha_beta_var*. This corroborates the theoretical results presented in Sec. 3.1 that predict a higher logarithmic decrement for the groove pattern *alpha_beta_var* compared to *beta_var* for the same radial clearance C . The experimental results presented in Fig. 15 for rotor *alpha_beta_hg_var* show that the sub-synchronous motion amplitude recorded at the back bearing exceeds the synchronous amplitude at a rotational speed of 173 krpm, indicating the onset of instability. At this speed, the experiment was stopped in order to avoid failure of the prototype. Note that all rotors have been balanced down to levels so that the maximum vibration amplitudes across the complete rotor speed range are well below 10% of the nominal bearing clearance.

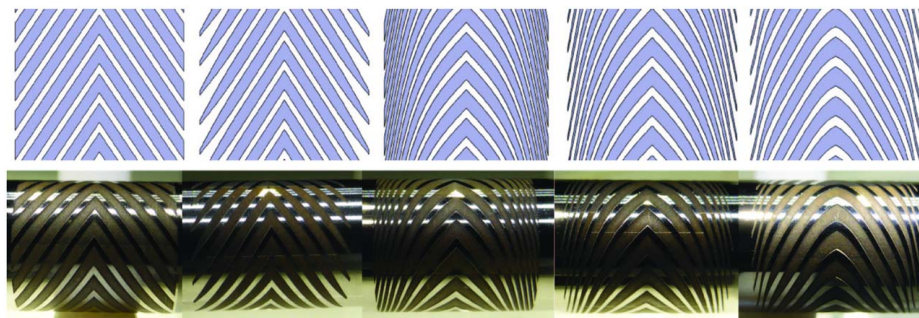


Fig. 9 Comparison of groove designs in CAD and in real after laser etching onto rotors. From left to right: classic, alpha_var, beta_var, alpha_beta_var, and alpha_beta_hg_var.

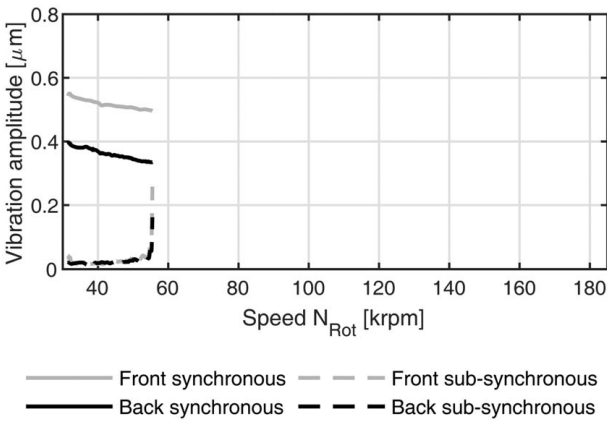


Fig. 11 Experimentally captured synchronous and sub-synchronous motion amplitudes of rotor classic

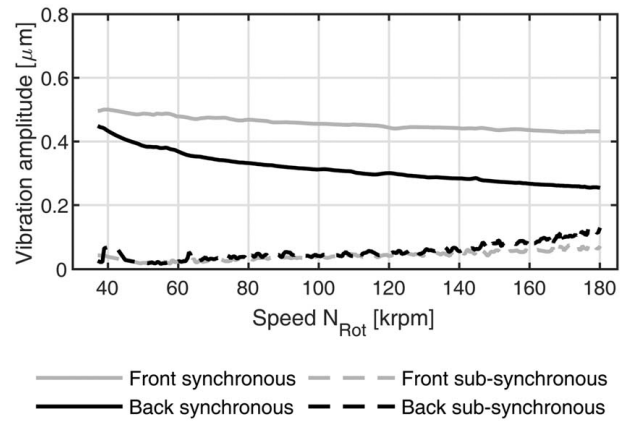


Fig. 14 Experimentally captured synchronous and sub-synchronous motion amplitudes of rotor alpha_beta_var

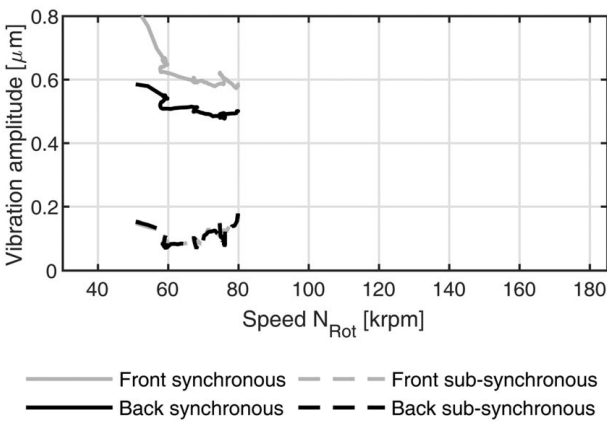


Fig. 12 Experimentally captured synchronous and sub-synchronous motion amplitudes of rotor alpha_var

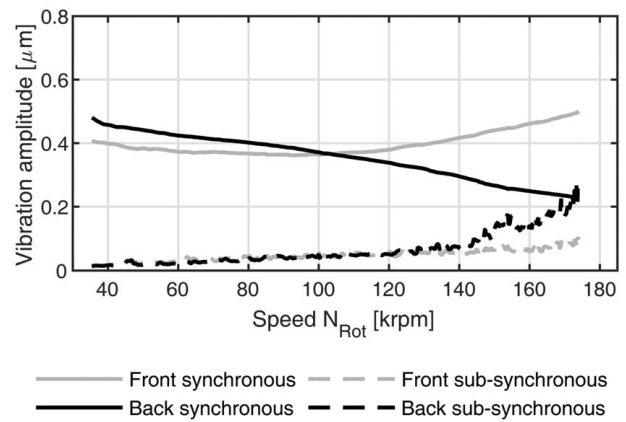


Fig. 15 Experimentally captured synchronous and sub-synchronous motion amplitudes of rotor alpha_beta_hg_var

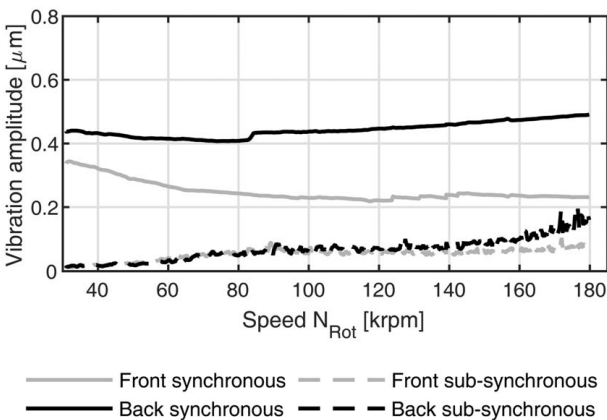


Fig. 13 Experimentally captured synchronous and sub-synchronous motion amplitudes of rotor beta_var

3.5 Repeatability of the Experimental Results. The rotor shafts used for this research paper have been manufactured from steel and have not been coated with a surface treatment. Their life-span is therefore limited due to rotor–bushing contact below lift-off speed. Nonetheless, each shaft has been tested several times and the appearance of sub-synchronous vibrations is repeatable for every

run and rotor configuration. To give an idea of the variation, the determined speed of instability onset for the rotor *classic* has been 59 krpm, 60 krpm, and 56 krpm. This corresponds to an average SIO of 58.33 krpm. The root-mean-square-error of the variation in the measured SIO for rotor *classic* is 1.7 krpm, confirming a very good repeatability of the experimental data.

3.6 Comparison of Predicted and Experimental Results. To account for the slight deviation between the measured bearing clearance of the tested rotors (refer to Table 6) and the design bearing clearance of $C = 8.2 \mu\text{m}$, the rotordynamic stability predictions were repeated in order to compare them to the experimentally determined speeds of instability onset. Furthermore, to account for measurement uncertainties on the measured rotor and bushing diameter and manufacturing uncertainties of the groove patterns, an uncertainty analysis was performed.

The uncertainty analysis is performed by evaluating the whirl speed maps for each rotor considering an uncertainty on the bearing clearance of $\Delta C = \pm 0.4 \mu\text{m}$ and on the groove depth of $\Delta hg = \pm 1 \mu\text{m}$. In order to take interactions of the two uncertainties into account, five rotordynamic calculations were performed for the combinations of clearance and groove depth ranges as shown in Fig. 16. The results from the five evaluations then serve to predict the nominal, maximum and minimum speed of instability onset for each investigated rotor.

Figure 17 presents the whirl speed map for the cylindrical and conical forward and backward modes for the *classic* rotor

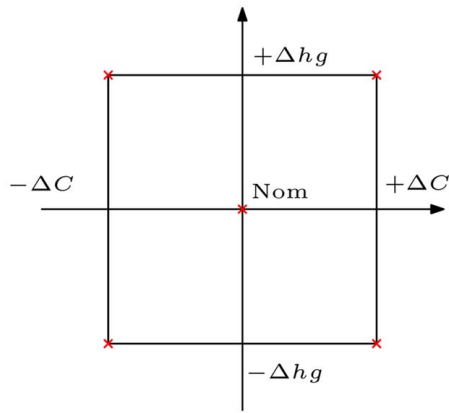


Fig. 16 Evaluated combinations of clearance uncertainty ΔC and groove depth uncertainty Δh_g in uncertainty analysis

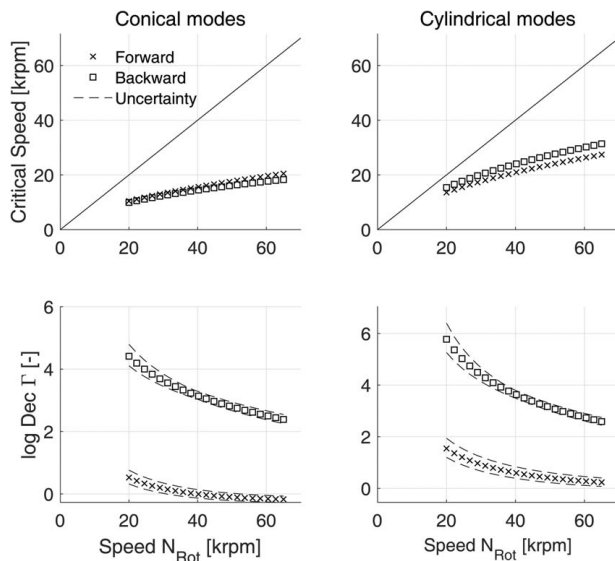


Fig. 17 Whirl speed map and evolution of logarithmic decrement Γ for rotor classic considering the uncertainty in bearing clearance and groove depth

configuration considering the uncertainty in bearing clearance and groove depth. The predicted whirl speed map suggests that the rotor does neither encounter a conical nor a cylindrical natural frequency in the tested speed range above 20 krpm. The cylindrical and conical backward modes do not cause concern since they are well damped and very rarely excited in general [25–27]. The results for the logarithmic decrement Γ suggest the expected instability to be a conical forward mode. To better capture the effect of the uncertainties in bearing clearance and groove depth on the speed of instability onset of the relevant conical forward mode, the evolution of the logarithmic decrement Γ as a function of rotor speed for rotor *classic* is plotted again in a larger format in Fig. 18. As suggested by the curves in Fig. 18, the nominal speed of instability onset (SIO) is predicted to be at around 40 krpm. This result is slightly lower than the previously predicted 44 krpm (refer to Table 4), since the actual clearance of the rotor is $C = 8.4 \mu\text{m}$ instead of $C = 8.2 \mu\text{m}$. When considering an uncertainty of $\Delta C = \pm 0.4 \mu\text{m}$ and $\Delta h_g = \pm 1 \mu\text{m}$, the expected speed range of instability onset is between 31 krpm and 52 krpm for the rotor *classic*.

Identical evaluations have been performed for the four shafts featuring enhanced groove geometries. The comparison between the experimentally measured and the predicted speed of instability

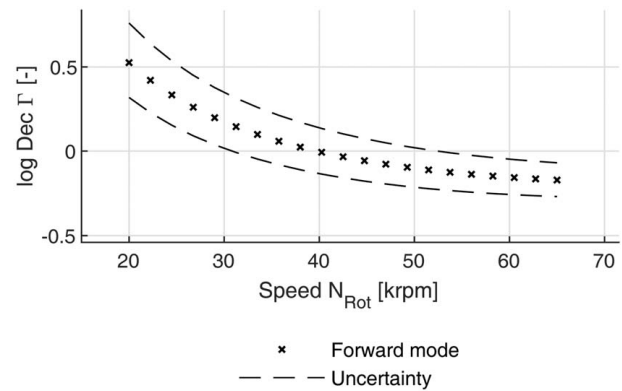


Fig. 18 Evolution of logarithmic decrement Γ for conical forward mode of rotor classic

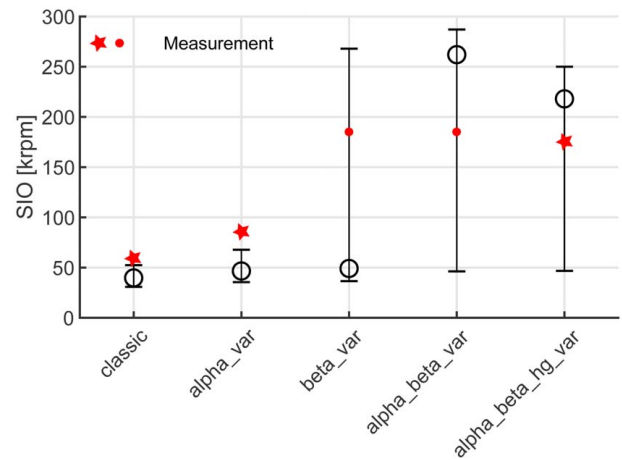


Fig. 19 Comparison of predicted and measured speed of instability onset. The circles represent the nominal onset of instability and the error bars the maximum and minimum values resulting from the measurement uncertainty. The stars represent experimentally observed instability, while the dots represent maximum achieved speed with no observed instability.

onset for all investigated rotors is summarized in Fig. 19. The bars represent the minimum, nominal, and maximum predicted speed of instability onset, when considering the uncertainties in rotor/bushing diameter and groove depth. The stars represent the speed, where an instability was observed in the experiment, and the dots indicate the maximum achieved speed in the experiment with no clear onset of instability present yet. As suggested by the comparison of predicted and measured data presented in Fig. 19, the theoretical results slightly under-predict the experimentally obtained results for rotors *classic* and *alpha_var*, even when considering the uncertainty in clearance and groove depth. For the rotors with the groove patterns *beta_var* and *alpha_beta_var*, the nominal speed of 180 krpm was predicted to be achievable, which was experimentally confirmed. Rotor *alpha_beta_hg_var* is suggested to have the highest performance according to the theoretically predicted results. The experimental data however suggests the performance of this rotor to be lower compared to rotors *beta_var* and *alpha_beta_var*. In general, the performance predictions of all rotors are slightly lower compared to the experimental results, except for rotor *alpha_beta_hg_var*.

Assuming a Gaussian distribution within the uncertainty range for the SIO presented in Fig. 19 enables the evaluation of the probability to reach a certain rotational speed for each rotor. The

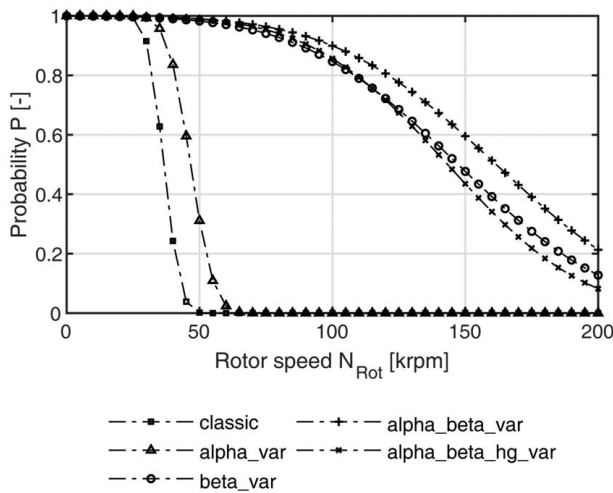


Fig. 20 Probability to reach a certain rotor speed for the five investigated groove geometries

probability for each rotor, assuming the uncertainty range to be equivalent to five times the standard deviation of the Gauss distribution, is presented in Fig. 20. It is evident that the probability to reach a certain rotational speed decreases with increasing rotor speed for all rotors. Furthermore, the results suggest that the probability for rotors *classic* and *alpha_var* to reach a speed higher than 60 krpm is negligible, whereas it is substantially larger for the rotors featuring more advanced groove geometries. Furthermore, the groove pattern *alpha_beta_var* is suggested to yield the highest probability to achieve a certain rotor speed, which makes this pattern the most promising one among the investigated ones.

The experimental results clearly suggest that enhanced groove geometries are able to significantly increase the stability threshold of the rotor-bearing system. Compared to a classically grooved rotor that becomes unstable at a rotational speed of 56 krpm, the application of enhanced grooves on the same rotor with the same nominal bearing clearance allows to reach a speed of 180 krpm, representing an increase by more than a factor of three of the SIO.

4 Conclusions

The potential of enhanced grooves to increase the stability threshold of HGJBs has been investigated theoretically and experimentally. The theoretical analysis suggested a rotor with enhanced groove geometry to have a higher stability threshold, which would allow for a higher rotational speed before instability onset compared to a classically grooved rotor featuring the same radial bearing clearance. The experimental results corroborated the theoretical results and demonstrated the stabilizing effect of enhanced groove geometries by achieving a rotational speed that is more than three times as high as the one achieved with the classically grooved baseline rotor featuring the same radial bearing clearance. Furthermore, it was found that the potential clearance increase offered by enhanced groove geometries is strongly dependent on the rotor mass, the transverse moment of inertia, and the relative location of the center of mass of the rotor.

The rotordynamic models presented in this paper reliably predict the onset of instability for rotors with enhanced groove geometries when measurement uncertainties in the bearing clearance and groove depth are considered in the theoretical analysis. It is evident that the manufacturing process of rotors and bushing, as well as the laser etching process, yields many more uncertainties than the two that have been considered. Further uncertainties could possibly stem from the groove angle, groove width, rotor and bearing roundness, extrapolated groove edge and land regions, transverse and polar rotor inertia as well as rotor mass.

The error bars presented in Fig. 19 suggest a rather large uncertainty range for the expected speed of instability onset when taking the manufacturing tolerances into account. This is due to the flat progression of the logarithmic decrement with rotational speed, as can be seen in Fig. 18. The progression of the logarithmic decrement as a function of the rotational speed is strongly dependent on the rotor mass, the transverse moment of inertia, and the relative location of the center of mass of the rotor. Even though the uncertainty range is large due to the properties of the rotor used for this investigation, Fig. 20 clearly demonstrates the significant increase in the probability to reach a certain rotor speed when applying enhanced groove designs. A rotor with more favorable design properties might offer even larger benefits when using enhanced groove geometries, as has been shown by Schiffmann [12].

Both the theoretical and experimental results have shown that the rotor *beta_var*, featuring enhanced grooves with only a variable groove angle β but with a constant groove width ratio α and a constant groove depth ratio H , represents a good trade-off between performance increase and design/manufacturing costs.

Acknowledgment

The authors acknowledge the funding by the Swiss National Science Foundation, grant PYAPP2_154278/1.

Conflict of Interest

There are no conflicts of interest.

Nomenclature

c	= bearing damping (N s m^{-1})
l	= bearing distance (m)
p	= pressure (Pa)
s	= rotordynamic system eigenvalue (s^{-1})
B	= system damping matrix (N s m^{-1})
C	= radial bearing clearance (m)
D	= bearing diameter (m)
H	= groove depth ratio, h_g/C
K	= system stiffness matrix (N m^{-1})
L	= bearing length (m)
M	= normalized system inertia matrix
P	= probability
R	= bearing radius (m)
Z	= bearing impedance (N m^{-1})
\bar{C}	= non-dimensional damping, $cCa/(DLp_{\text{amb}})$
\bar{K}	= non-dimensional stiffness, $KC/(DLp_{\text{amb}})$
\bar{P}	= normalized pressure, $p/(p_{\text{amb}})$
\bar{P}	= normalized fluid film pressure
c_s	= bearing parameter
f_i	= geometrical bearing parameters
h_g	= groove depth (m)
m_R	= rotor mass (kg)
p_{amb}	= ambient pressure (Pa)
J_P	= polar rotor inertia (kg m^2)
J_T	= transverse rotor inertia (kg m^2)
N_{Rot}	= rotor speed (min^{-1})
T_{amb}	= ambient temperature (K)

Greek Symbols

α	= groove width ratio
β	= groove angle (deg)
γ	= groove width ratio
Γ	= logarithmic decrement
ε	= bearing eccentricity ratio
Λ	= compressibility number
μ	= viscosity (Pa s)

σ = squeeze film number
 ω_{Rot} = angular frequency (rad s⁻¹)
 Ω = whirl ratio

Appendix A: Details of the Rotordynamic Model

The matrices for the rotordynamic equation of motion (Eq. (1)) are given as follows:
 The system inertia matrix:

$$M = \begin{bmatrix} m_{\text{Rot}} & 0 & 0 & 0 \\ 0 & m_{\text{Rot}} & 0 & 0 \\ 0 & 0 & J_T & 0 \\ 0 & 0 & 0 & J_T \end{bmatrix}$$

The system stiffness matrix:

$$K = \begin{bmatrix} K_{xxa} + K_{xxb} & K_{xya} + K_{xyb} & K_{xxa}l_a - K_{xxb}l_b & -K_{xya}l_a + K_{xyb}l_b \\ K_{yx_a} + K_{yx_b} & K_{yya} + K_{yyb} & K_{yx_a}l_a - K_{yx_b}l_b & -K_{yya}l_a + K_{yyb}l_b \\ K_{xxa}l_a - K_{xxb}l_b & K_{xya}l_a - K_{xyb}l_b & K_{xxa}l_a^2 + K_{xxb}l_b^2 & -K_{xya}l_a^2 - K_{xyb}l_b^2 \\ -K_{yx_a}l_a + K_{yx_b}l_b & K_{yya}l_a - K_{yyb}l_b & -K_{yx_a}l_a^2 - K_{yx_b}l_b^2 & K_{yya}l_a^2 + K_{yyb}l_b^2 \end{bmatrix}$$

The system damping matrix:

$$B = C + G$$

with

$$C = \begin{bmatrix} C_{xxa} + C_{xxb} & C_{xya} + C_{xyb} & C_{xxa}l_a - C_{xxb}l_b & -C_{xya}l_a + C_{xyb}l_b \\ C_{yx_a} + C_{yx_b} & C_{yya} + C_{yyb} & C_{yx_a}l_a - C_{yx_b}l_b & -C_{yya}l_a + C_{yyb}l_b \\ C_{xxa}l_a - C_{xxb}l_b & C_{xya}l_a - C_{xyb}l_b & C_{xxa}l_a^2 + C_{xxb}l_b^2 & -C_{xya}l_a^2 - C_{xyb}l_b^2 \\ -C_{yx_a}l_a + C_{yx_b}l_b & C_{yya}l_a - C_{yyb}l_b & -C_{yx_a}l_a^2 - C_{yx_b}l_b^2 & C_{yya}l_a^2 + C_{yyb}l_b^2 \end{bmatrix}$$

and

$$G = \begin{bmatrix} 0 & 0 & 0 & 0 \\ 0 & 0 & 0 & 0 \\ 0 & 0 & 0 & -J_P\omega_{\text{Rot}} \\ 0 & 0 & J_P\omega_{\text{Rot}} & 0 \end{bmatrix}$$

Appendix B: Modified Reynolds Equation

The coefficients for the modified Reynolds equation (Eq. (5)) are summarized as follows:

$$\bar{h}_r = \frac{h_r}{C}$$

$$\bar{h}_g = 1 + \frac{h_g}{C}$$

$$H = \frac{h_g}{C}$$

$$g_1 = \bar{h}_g^3 \bar{h}_r^3$$

$$g_2 = (\bar{h}_g^3 - \bar{h}_r^3)^2 \alpha (1 - \alpha)$$

$$(1 - \alpha) \bar{h}_g^3 + \alpha \bar{h}_r^3$$

$$c_s = -\frac{6\mu\Omega_{\text{Rot}}R^2}{p_{\text{amb}}h_0^2} \alpha (1 - \alpha) (H - 1) \sin \beta$$

$$f_1 = \frac{g_1 + g_2 \sin \beta}{g_3}$$

$$f_2 = \frac{g_2 \sin \beta \cos \beta}{g_3}$$

$$f_3 = \frac{g_1 + g_2 \cos \beta}{g_3}$$

$$f_4 = \frac{\bar{h}_g^3 - \bar{h}_r^3}{g_3}$$

$$f_5 = \alpha \bar{h}_g + (1 - \alpha) \bar{h}_r \quad \Lambda = \frac{6\mu\Omega_{\text{Rot}}}{p_{\text{amb}}} \left(\frac{R}{h_r} \right)^2$$

$$\sigma = \frac{12\mu\Omega_{\text{Rot}}\gamma}{p_{\text{amb}}} \left(\frac{R}{h_r} \right)^2$$

References

- [1] Belforte, G., Colombo, F., Raparelli, T., and Viktorov, V., 2008, "High-Speed Rotor With Air Bearings Mounted on Flexible Supports: Test Bench and Experimental Results," *ASME J. Tribol.*, **130**(2), p. 021103.
- [2] Waumans, T., Peirs, J., Al-Bender, F., and Reynaerts, D., 2011, "Aerodynamic Journal Bearing With a Flexible, Damped Support Operating at 7.2 Million Dn," *J. Micromech. Microeng.*, **21**(10), p. 104014.
- [3] Waumans, T., Peirs, J., Al-Bender, F., and Reynaerts, D., 2009, "Design, Optimisation and Testing of a High-Speed Aerodynamic Journal Bearing With a Flexible, Damped Support," Technical Digest PowerMEMS., Washington, DC, Dec. 1–4, pp. 83–86.
- [4] Miyanaga, N., and Tomioka, J., 2016, "Effect of Support Stiffness and Damping on Stability Characteristics of Herringbone-Grooved Aerodynamic Journal Bearings Mounted on Viscoelastic Supports," *Tribol. Int.*, **100**, pp. 195–203.
- [5] Tomioka, J., and Miyanaga, N., 2008, "Measurement of Dynamic Properties of O-Rings and Stability Threshold of Flexibly Supported Herringbone Grooved Aerodynamic Journal Bearings," *Tribol. Online*, **3**(7), pp. 366–369.
- [6] Tomioka, J., and Miyanaga, N., 2013, "Stability Threshold of Herringbone-Grooved Aerodynamic Journal Bearings With External Stiffness and Damping Elements," *J. Adv. Mech. Des. Syst. Manuf.*, **7**(6), pp. 876–887.
- [7] Bättig, P., and Schiffmann, J., 2019, "Data-Driven Model for the Dynamic Characteristics of O-Rings for Gas Bearing Supported Rotors," *ASME J. Appl. Mech.*, **86**(8), p. 081003.
- [8] Somaya, K., Miyatake, M., Okubo, K., and Yoshimoto, S., 2015, "Threshold Speed of Instability of a Herringbone-Grooved Rigid Rotor With a Bearing Bush Flexibly Supported by Straight Spring Wires," Proceedings of ASME Turbo Expo 2015: Turbine Technical Conference and Exposition GT2015, Montreal, Quebec, Canada, June 15–19, p. V07AT31A015.
- [9] Yoshimoto, S., Miyatake, M., and Nagata, K., 2007, "Instability of Herringbone Grooved Aerodynamic Floating Bush Bearings Flexibly Supported by Foils With Hemispherical Bumps," Proceedings of ASME/STLE International Joint tribology Conference, San Diego, CA, Oct. 22–24, pp. 261–263.
- [10] Bättig, P., and Schiffmann, J., 2020, "Flexible Support for Gas Lubricated Bearing Bushings," *Tribol. Trans.*, **63**(2), pp. 1–27.
- [11] Ikeda, S., Arakawa, Y., Hishida, N., Hirayama, T., Matruoka, T., and Yabe, H., 2010, "Herringbone-Grooved Bearing With Non-Uniform Grooves for High-Speed Spindle," *Lubr. Sci.*, **22**(9), pp. 377–392.
- [12] Schiffmann, J., 2013, "Enhanced Groove Geometry for Herringbone Grooved Journal Bearings," *ASME J. Eng. Gas Turbines Power*, **135**(10), p. 102501.
- [13] Hashimoto, H., and Ochiai, M., 2008, "Optimization of Groove Geometry for Thrust Air Bearing to Maximize Bearing Stiffness," *ASME J. Tribol.*, **130**(3), p. 031101.
- [14] Yu, Y., Pu, G., Jiang, T., and Jiang, K., 2021, "Optimization of Herringbone Grooved Thrust Air Bearings for Maximum Load Capacity," *ASME J. Tribol.*, **143**(12), p. 121805.
- [15] Durillo, J. J., Nebro, A. J., Coello, C. A. C., Luna, F., and Alba, E., 2008, "A Comparative Study of the Effect of Parameter Scalability in Multi-Objective Metaheuristics," IEEE Congress on Evolutionary Computation (IEEE World Congress on Computational Intelligence), Hong Kong, China, June 1–6, IEEE, pp. 1893–1900.
- [16] Lund, J. W., 1968, "Calculation of Stiffness and Damping Properties of Gas Bearings," *ASME J. Lubr. Technol.*, **90**(4), pp. 783–803.
- [17] Gu, L., Guenat, E. P., and Schiffmann, J. A., 2020, "A Review of Grooved Dynamic Gas Bearings," *ASME Appl. Mech. Rev.*, **72**(1), p. 010802.
- [18] Iseli, E., Guenat, E. P., Tresch, R., and Schiffmann, J. A., 2020, "Analysis of Spiral-Grooved Gas Journal Bearings by the Narrow-Groove Theory and the Finite Element Method at Large Eccentricities," *ASME J. Tribol.*, **142**(4), p. 041802.
- [19] Guenat, E. P., and Schiffmann, J. A., 2020, "Dynamic Force Coefficients Identification on Air-Lubricated Herringbone Grooved Journal Bearing," *Mech. Syst. Signal Process.*, **136**, p. 106498.
- [20] Molyneaux, A., Leyland, G. B., and Favrat, D., 2010, "Environomic Multi-Objective Optimization of a District Heating Network Considering Centralized and Decentralized Heat Pumps," *Energy*, **35**(2), pp. 751–758.
- [21] Wagner, P., Wullemin, Z., Constantin, D., Diethelm, S., Herle, J. V., and Schiffmann, J., 2020, "Experimental Characterization of a Solid Oxide Fuel Cell Coupled to a Steam-Driven Micro Anode Off-Gas Recirculation Fan," *Appl. Energy*, **262**, p. 114219.
- [22] Vohr, J., and Chow, C., 1965, "Characteristics of Herringbone-Grooved, Gas-Lubricated Journal Bearings," *ASME J. Basic Eng.*, **87**(3), pp. 568–576.
- [23] Fuller, D., 1969, "A Review of the State-of-the-Art for the Design of Self-Acting Gas-Lubricated Bearings," *ASME J. Lubr. Technol.*, **91**(1), pp. 1–16.
- [24] Darlow, M. S., 1989, *Balancing of High-Speed Machinery*, F. F. Ling and W. H. Hart, eds., 1st ed., Springer, New York, pp. 81–106.
- [25] Greenhill, L., and Cornejo, G., 1995, "Critical Speeds Resulting From Unbalance Excitation of Backward Whirl Modes," ASME Design Engineering Technical Conferences—Part B, Boston, MA, Sept. 17–20, Vol. 3, pp. 991–1000.
- [26] Jahromi, A., Bhat, R., and Xie, W.-F., 2014, "Forward and Backward Whirling of a Rotor With Gyroscopic Effect," *Vibration Engineering and Technology of Machinery: Proceedings of VETOMAC X 2014*, University of Manchester, UK, Sept. 9–11, Vol. 23, pp. 879–887.
- [27] Pedersen, P., 1972, "On Forward and Backward Precession of Rotors," *Ingenieur-Archiv*, **42**(1), pp. 26–41.